

Self-Assembled Heteroepitaxial Oxide Nanocomposite for Photoelectrochemical Solar Water Oxidation

Seungho Cho,[†] Ji-Wook Jang,[‡] Leigang Li,[§] Jie Jian,^{||} Haiyan Wang,^{§,||} and Judith L. MacManus-Driscoll^{*,†}

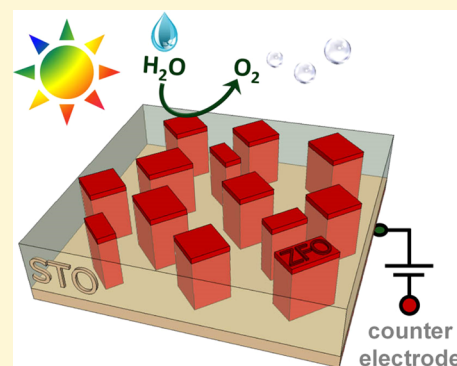
[†]Department of Materials Science and Metallurgy, University of Cambridge, 27 Charles Babbage Road, Cambridge, CB3 0FS, United Kingdom

[‡]Helmholtz-Zentrum Berlin für Materialien und Energie GmbH, Institute for Solar Fuels, Hahn-Meitner-Platz 1, Berlin 14109, Germany

[§]Department of Materials Science and Engineering and ^{||}Department of Electrical and Computer Engineering, Texas A&M University, College Station, Texas 77843, United States

Supporting Information

ABSTRACT: We report on spontaneously phase ordered heteroepitaxial SrTiO₃ (STO):ZnFe₂O₄ (ZFO) nanocomposite films that give rise to strongly enhanced photoelectrochemical solar water oxidation, consistent with enhanced photo-induced charge separation. The STO:ZFO nanocomposite yielded an enhanced photocurrent density of 0.188 mA/cm² at 1.23 V vs a reversible hydrogen electrode, which was 7.9- and 2.6-fold higher than that of the plain STO film and ZFO film cases under 1-sun illumination, respectively. The photoelectrode also produced stable photocurrent and Faradaic efficiencies of H₂ and O₂ formation that were more than 90%. Incident-photon-to-current-conversion efficiency measurements, Tauc plots, Mott–Schottky plots, and electrochemical impedance spectroscopy measurements proved that the strongly enhanced photogenerated charge separation resulted from vertically aligned pseudosingle crystalline components, epitaxial heterojunctions, and a staggered band alignment of the components of the nanocomposite films. This study presents a completely new avenue for efficient solar energy conversion applications.



1. INTRODUCTION

Owing to their higher stability than other semiconductors, metal oxides are promising materials for photoelectrochemical (PEC) applications, especially for photoanodes performing the “oxidation” half-reaction in aqueous electrolytes.^{1,2} In addition, the large range of metal cations give rise to a wide diversity of optoelectronic properties related to the different cation oxidation states, crystal structures, and electronic configurations.³ A large variety of binary and ternary oxides have been investigated for photoanode materials. In general, however, achieving a set of desired properties in simple component materials is exceedingly difficult. Commonly, combinations of two or more components made of simple materials have been employed for superior properties. On the basis of the possibility of extension of the spectral range of light absorption and efficient photoinduced charge separation, “heterostructured” metal oxide photoelectrodes have been widely developed for their enhanced PEC efficiencies,³ such as SrTiO₃/α-Fe₂O₃,⁴ α-Fe₂O₃/ZnFe₂O₄,⁵ TiO₂/ZnFe₂O₄,⁶ TiO₂/WO₃,⁷ SrTiO₃/ZnFe₂O₄,⁸ and ZnO/ZnFe₂O₄.⁹

Since phase-ordered heteroepitaxial oxide nanocomposites were first reported,^{10–12} the unique structural features of this class of materials have led to their wide use in functional

areas.^{13–17} With respect to solar energy conversion applications, these self-organizing systems have the following remarkable features, in addition to the generic characters of heterostructures: (i) Phase-separated components are usually vertically aligned on substrates [i.e., vertical nanopillar (or nanowire) in a matrix].¹⁸ Thus, these heterostructures have short diffusion pathways of photoinduced charge carriers in the radial direction before charge separation and unidirectional carrier transport along the axial direction of the one-dimensional components. (ii) Each component is pseudosingle crystalline with significantly reduced grain boundaries; hence the systems possess potentially reduced charge carrier trap sites. (iii) Epitaxial interfaces between two separated phases have fewer crystallographic defects than other heterojunction interfaces (e.g., polycrystalline–single crystalline or polycrystalline–polycrystalline heterojunctions). Therefore, together these three salient features give great prospects for improving the overall photogenerated charge transfer efficiency. However, to the best of our knowledge, a study on a self-assembled

Received: January 11, 2016

Revised: April 11, 2016

Published: April 13, 2016

heteroepitaxial oxide nanocomposite for solar energy conversion has not yet been reported.

In this study, SrTiO₃ (STO):ZnFe₂O₄ (ZFO) thin films were synthesized and used as a model system for solar energy conversion applications of self-assembled heteroepitaxial nanocomposites because STO and ZFO are widely studied photocatalysts and have different crystal structures [perovskite for STO (*Pm* $\bar{3}$ *m* space group) and spinel for ZFO (*Fd* $\bar{3}$ *m*) with a staggered energy band alignment].^{8,19,20} The STO:ZFO nanocomposites were three-dimensional epitaxial heterostructures where vertically aligned ZFO nanopillars on STO substrates were embedded in STO matrices. The nanocomposites exhibited a significantly enhanced PEC efficiency in both the UV- and visible-light regions compared with individual STO and ZFO films. A series of measurements resulting in Tauc plots, Mott–Schottky plots, and Nyquist plots indicate that more efficient transport of photogenerated charge carriers in self-assembled heteroepitaxial nanocomposites is the origin of the strong enhancement of the solar energy conversion efficiency observed.

2. EXPERIMENTAL SECTION

2.1. Film Fabrication. Films were grown on STO(001) substrates by pulsed laser deposition (PLD) with a KrF laser ($\lambda = 248$ nm) with a fluence of 0.75 J/cm² and a repetition rate of 1 Hz. A polycrystalline STO target, a polycrystalline ZFO target, and a polycrystalline target containing STO and ZFO of 50:50 molar ratio were used for STO films, ZFO films, and STO:ZFO nanocomposite films, respectively. During deposition, the substrate temperature was 810 °C and the O₂ pressure was fixed at 0.2 mbar. The samples were postannealed at 685 °C for 1 h under 400 mbar O₂. For the self-assembled nanocomposite photoelectrodes, a STO:ZFO nanocomposite layer (nominal thickness \sim 385 nm) followed by a ZFO layer (nominal thickness \sim 15 nm) was in situ deposited on a SrRuO₃ (SRO)-buffered STO substrate. The depositions were done without breaking vacuum by rotating a target carousel to avoid contamination at the interfaces between the different layers. For an Fe-doped STO film (for a control experiment), we used the same deposition procedure, with a polycrystalline target containing α -Fe₂O₃ and STO. SRO (as an electrode and for epitaxial growth of photoactive films)-buffered STO substrates were used for PEC measurements. The SRO-buffered STO substrates were prepared by PLD with a substrate (STO) temperature of 650 °C and an O₂ pressure of 0.2 mbar using a polycrystalline SRO target. A nominal thickness of each SRO layer is 38 nm. The SRO-buffered STO substrate was postannealed at 450 °C for 1 h under 400 mbar O₂ prior to deposition of the photoactive films.

2.2. Characterizations. The phase and the crystalline nature of the films were investigated by ω – 2θ and asymmetric X-ray diffraction (XRD) on a PANalytical Empyrean high-resolution X-ray diffractometer. For investigating in-plane orientation, φ -scans were obtained by 360° in-plane sample rotation around (202) peaks of the films and substrates. Reciprocal space maps (RSMs) were collected about the (002) and (103) of STO substrates. The ω – 2θ diffraction peaks and RSM peaks were used to calculate the lattice parameters of the films. Transmission electron microscopy (TEM) was performed using a FEI Tecnai G2 F20 microscope, operated at 200 kV. To determine film surface morphology, atomic force microscopy (AFM) (Multimode 8 SPM with Nanoscope V controller) was performed. For optical absorption measurement, double-side-polished STO substrates were used. UV–visible absorption spectra were obtained using an Agilent 8453.

2.3. Photoelectrochemical Measurements. The current–potential (I – V) curves of PEC water oxidation were obtained in a 1 M NaOH solution purged with nitrogen using a platinum foil counter electrode, a Ag/AgCl (3 M NaCl) reference electrode, and a potentiostat. The photocathodes were front-side-illuminated with an AM 1.5 solar simulator (100 mW/cm², Newport Oriel 91160). The

evolved amounts of H₂ and O₂ were analyzed by a gas chromatograph (HP5890) with a thermal conductivity detector, and a molecular sieve 5-A column. Incident-photon-to-current-conversion efficiency (IPCE) was measured using the 150 W Xe lamp and a monochromator. The IPCEs were measured at 1.23 V vs a reversible hydrogen electrode (RHE) in the same solution. Potentiostatic electrochemical impedance spectroscopy was conducted at the dc potential of 1.23 V vs RHE with an ac potential frequency range of 5000–0.1 Hz under 1-sun illumination. Mott–Schottky analysis was carried out at a dc potential range from –1.5 to +1.5 V vs Ag/AgCl with the ac potential frequency 5 kHz and an amplitude of ac potential of 50 mV under dark condition.

3. RESULTS AND DISCUSSION

Self-assembled heteroepitaxial oxide nanocomposites were synthesized by PLD. A polycrystalline target containing STO and ZFO of 50:50 molar ratio was used for PLD. Spontaneous phase ordering of perovskite STO and spinel ZFO occurred during deposition. Parts a and b of Figure 1 show AFM images of the nanocomposite film surface (topography and phase contrast images, respectively) clearly showing faceted phase islands dispersed in a matrix of another phase. It is inferred that the islands and matrix are ZFO and STO, respectively, from homoepitaxy of STO on STO substrate (i.e., perfect wetting). Cross-sectional TEM was used to further confirm the phases and their orientation in the vertical direction. The low-magnification TEM image shown in Figure 1c reveals that the ZFOs are indeed the nanopillars (islands) surrounded by the flat STO matrix. Figure 1d displays a high-resolution TEM image around the interface between STO and ZFO, showing that the matrix and nanopillars have single-crystalline nature with heteroepitaxial interfaces. The self-assembled STO:ZFO nanocomposite film is schematically illustrated in Figure 1e on the basis of the AFM and TEM analyses.

The crystalline nature of the nanocomposite was also studied using four-circle X-ray diffraction (XRD). The ω – 2θ scans (Figure 2a,b) of the STO:ZFO film show STO and ZFO phase separation, and their high degree of crystallographic orientation is revealed by (00 l) diffraction peaks without traces of other phases or orientations. The matrix STO(00 l) peaks deviate from the substrate STO(00 l) peaks, indicating that the STO component of the nanocomposite film is strained by the ZFO component [Figure 2b; for comparison, the ω – 2θ scan and the reciprocal space map (RSM) around STO(002) of a bare STO substrate are provided in the Supporting Information, Figure S1a].¹³ XRD analysis of asymmetrical reflections confirmed epitaxial growth. The φ -scans around STO(202) and ZFO(404) of the nanocomposite film display a set of four peaks, 90° apart, at the same φ -angles, indicating [100]–STO(001)//[100]ZFO(001) epitaxial relationships (i.e., growth on substrate in a cube-on-cube fashion). Further structural information is obtained by the RSM around STO(103) for the STO:ZFO film on the STO substrate (Figure 2d). The ZFO(206) peak is observed in a lower q_z region than the (103) peak of the STO matrix that is in proximity to the high-intensity (103) peak of STO substrate. For comparison, RSM around STO(103) of the bare STO substrate is included in the Supporting Information (Figure S1b). The out-of-plane lattice parameters of ZFO and STO matrix are calculated as 8.386 and 3.918 Å, respectively, corresponding to compression of ZFO (0.56%) and expansion of STO (0.33%) [$a = 8.433$ Å for bulk ZFO (JCPDS # 65-3111) and $a = 3.905$ Å for bulk STO (JCPDS # 35-0734)]. The in-plane lattice parameters of ZFO and STO matrix are

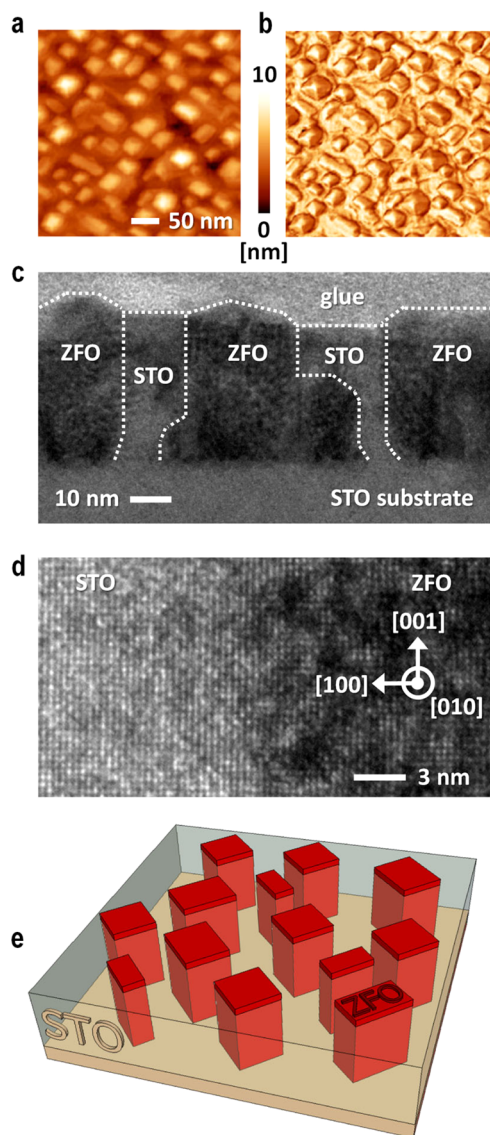


Figure 1. (a and b) AFM images of an STO:ZFO nanocomposite film (topography and phase contrast image, respectively). (c) Cross-sectional TEM image of the STO:ZFO nanocomposite film on STO substrate. (d) High-resolution cross-sectional TEM image around the interface between STO and ZFO phases. (e) Typical depiction of a self-assembled heteroepitaxial nanocomposite, in which the ZFO nanopyllars are embedded in an STO matrix.

identified as 8.435 and 3.897 Å. ZFO has a small tensile strain (0.02%) and STO has a compressive strain (0.20%) along the in-plane direction, which indicates that vertical strain control dominates in the nanocomposite film.¹³ Figure 2e shows a crystallographic model of a vertical interface between the STO and the ZFO on the STO substrate.

The PEC water oxidation properties of a self-assembled STO:ZFO nanocomposite film were investigated by growing the nanocomposite film on conducting perovskite SRO (nominal thickness of 38 nm)-buffered STO substrates. The SRO layers were required for photogenerated charge carrier extraction.²¹ ZFO, STO, and Fe-doped STO photoelectrodes were also fabricated for control experiments. The nominal thicknesses of the photoactive films were ~400 nm. Figure 3a shows current–voltage (I – V) curves for the photoelectrodes in a 1 M NaOH solution under chopped 1-sun illumination. ZFO

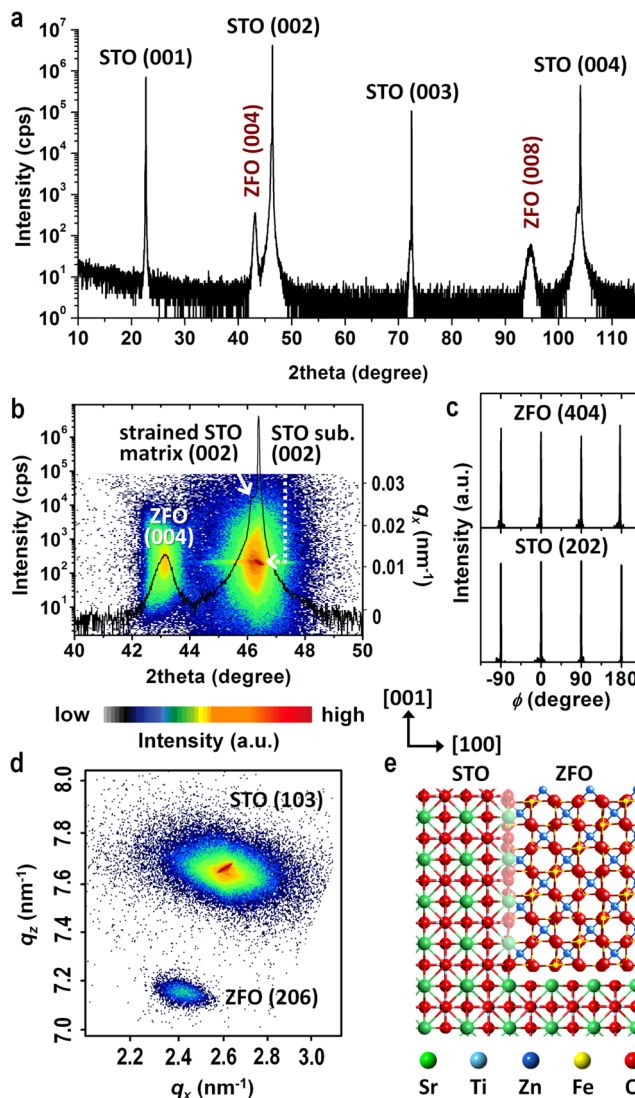


Figure 2. (a and b) ω – 2θ Scan of the STO:ZFO nanocomposite film. The inset of part b is the RSM around the (002) reflections. (c) The 360° ϕ -scans of the (202) peak of STO and the (404) peak of ZFO. (d) RSM around the STO(103) reflections. (e) Crystallographic model of a STO:ZFO nanocomposite around an interface between STO and ZFO on STO substrate.

and STO showed a photocurrent density of 0.052 and 0.021 mA/cm² at 1.23 V vs RHE, respectively. For self-assembled nanocomposite photoelectrodes, we in situ deposited the STO:ZFO nanocomposite layer (nominal thickness ~385 nm) followed by the ZFO layer (nominal thickness ~15 nm), on a SRO-buffered STO substrate. The depositions were done without breaking the vacuum by rotating a target carousel to avoid contamination at the interfaces between the different layers. The inset of Figure 3b shows a schematic cross-section of the STO:ZFO nanocomposite photoelectrode. The structural features of the STO:ZFO nanocomposite films on the SRO-buffered STO substrates are almost the same as those of the STO:ZFO nanocomposite films on STO substrates, such as crystallographic orientations, lattice parameters, and ZFO nanocolumn widths. First, XRD ω – 2θ scans show the same crystallographic orientations with almost the same out-of-plane lattice parameter (8.387 Å of the ZFO phase) on SRO-buffered STO as that of the ZFO phase (8.386 Å) in the STO:ZFO

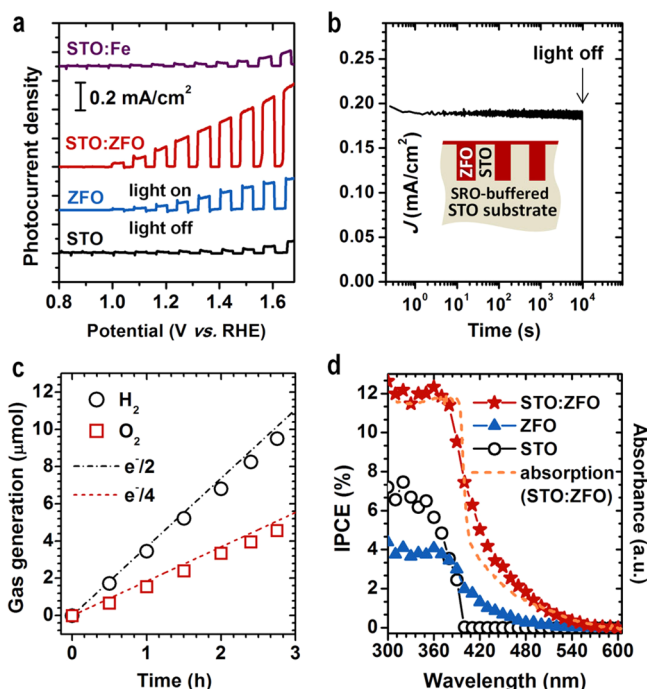


Figure 3. (a) Polarization curves of STO, ZFO, STO:ZFO nanocomposite, and 2 atom % Fe-doped STO films on SrRuO₃-buffered STO substrates in 1 M NaOH solution under chopped 1-sun illumination. (b) Current–time curve of the STO:ZFO nanocomposite film kept at 1.23 V vs RHE in the solution under 1-sun illumination. (c) Amounts of H₂ and O₂ gas evolved by the reaction, matching the number of charges measured. The theoretical lines were calculated according to Faraday's law of electrolysis. (d) IPCE measurements for the photoelectrodes carried out at 1.23 V vs RHE and an absorption spectrum of STO:ZFO nanocomposite film.

nanocomposite films on the STO substrates [Figures 2a,b and S2a (Supporting Information)]. An XRD RSM around the (103) asymmetric peak was obtained to further investigate the crystal structures (Figures S2b in the Supporting Information). The SRO(103) and the film (103) peaks are observed in the lower q_z regions than the high-intensity (103) peak of the STO substrate. The q_x positions for SRO(103) are, within the error range, the same as those of the (103) peaks for the STO substrates, which indicates that the SRO layers were fully strained along the in-plane direction, i.e., the same in-plane lattice parameter of SRO as that of STO substrates. The in-plane lattice parameter of the ZFO phase in the STO:ZFO film on the SRO-buffered STO substrate (8.434 Å) is also almost the same as that of the ZFO phase in the STO:ZFO film without an SRO-buffer layer (8.435 Å). In addition, AFM images indicate the similar dimensions and shapes of ZFO islands (i.e., ZFO columns) (Figure S2c in the Supporting Information). On the basis of the results of XRD and AFM measurements, we can, therefore, deduce that the STO:ZFO films with and without the SRO-buffer layer have almost the same structural features. The STO:ZFO nanocomposite yielded an enhanced photocurrent density of 0.188 mA/cm² at 1.23 V vs RHE. This current represents more than a 7.9 and 2.6 times increase from the STO film and ZFO film cases, respectively. This photocurrent density value of the STO:ZFO nanocomposite is comparable to that of the microwave post-treated ZFO nanostructure photoanodes recently reported²² and an order of magnitude higher than those of nanostructured ZFO photoanodes and thin film ferrite photoanodes.^{22–25} Figure S3

in the Supporting Information shows an AFM image of the plain ZFO film surface. The surface roughness of the plain ZFO film was slightly higher (4.211 nm) than that (3.467 nm) of the ZFO:STO nanocomposite film. The surface areas of the films were comparable. Thus, we can rule out the possibility of a significant contribution of a surface area difference to the enhanced photocurrent densities of the nanocomposite film. The reasons for this efficiency enhancement resulting from the nanocomposite structure will be discussed later. A constant potential measurement was performed at 1.23 V vs RHE in the NaOH solution to examine the stability of photocurrent generated by the nanocomposite photoelectrodes. The current–time curve of STO:ZFO under continuous 1-sun illumination shows that the photocurrent was sustained for at least 3 h (Figure 3b). The amounts of evolved H₂ and O₂ gases were measured to confirm that the generated photocurrent results from water splitting. Faradaic efficiencies of more than 90% were obtained by comparing the amounts of evolved gases with the expected amounts from the generated photocurrents (Figure 3c). These results indicate that the STO:ZFO nanocomposite photoelectrode is of good stability and that the photogenerated charges are indeed used for water splitting.

To explore the possible origin of the PEC efficiency enhancement observed in the STO:ZFO nanocomposite films compared with individual STO and ZFO films, respectively, a series of additional measurements were performed. IPCEs at 1.23 V vs RHE in the same solution were measured to study the photoresponse of the photoanodes as a function of the wavelength of incident light (Figure 3d). The IPCE values were integrated with respect to the AM 1.5G spectrum. The resulting values for the photoanodes were added to the Supporting Information (Table S1) to compare with the corresponding steady-state photocurrents at 1.23 V vs RHE. The STO film exhibited no photoresponse under visible light because of its wide band gap. In contrast, the ZFO film and the STO:ZFO nanocomposite film both showed PEC activities under visible light ($\lambda \leq 560$ nm). UV light accounts for only 4% of the solar energy spectrum. Thus, the STO:ZFO nanocomposite film yielded a much higher photocurrent density than that of the STO film under the solar simulator. We cannot rule out the possibility that diffusion of Fe ions into the STO component during the deposition of the nanocomposite film. Thus, we performed the PEC activity test using a 2 atom % Fe-doped STO film synthesized through the same film growth process as the STO:ZFO nanocomposite photoelectrode. In contrast to the STO:ZFO nanocomposite case, a prominent enhancement in PEC activity was not observed with the Fe-doped STO film compared with the pure STO film (Figure 3a). Therefore, Fe ion diffusion to the STO that can lead to visible light absorption does not play a major role in the PEC activity enhancement of the STO:ZFO nanocomposite photoelectrode.

We now turn to the comparison of the STO:ZFO nanocomposite photoanode with the ZFO photoanode. The STO:ZFO nanocomposite exhibited higher IPCEs in both UV- and visible-light regions compared to ZFO (Figure 3d). The IPCE behaviors of the photoanodes followed the absorption spectra qualitatively, indicating that the majority of the absorbed light of different wavelengths contributed to photocurrent generation. Relative absorbance spectra of the ZFO film and the STO:ZFO nanocomposite film are provided in the Supporting Information (Figure S4). Relative absorbance of the STO:ZFO nanocomposite film was lower than that of the ZFO film. The result can be attributed to the reduction of the total

volume of the ZFO phase in the films. The energy band gaps of the films were determined using Tauc plots. The band gaps of the STO and ZFO components of the nanocomposite film are almost the same as those of the STO film (~ 3.2 eV) and the ZFO film (~ 1.9 eV), respectively (Figure 4a,b). To investigate

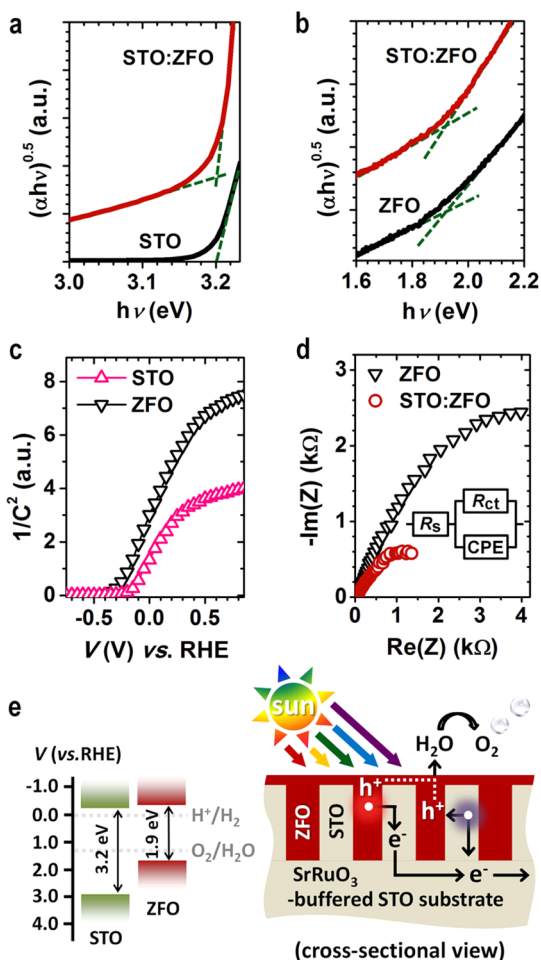


Figure 4. (a and b) Tauc plots of STO, ZFO, and STO:ZFO nanocomposite films. (c) Mott–Schottky plots of STO and ZFO. (d) Nyquist plots of EIS results of the ZFO and STO:ZFO nanocomposite photoanodes at 1.23 V vs RHE. The inset shows an equivalent circuit model for the photoanodes. (e) Schematic illustrations of band structures for STO and ZFO and photoelectrochemical performance of STO:ZFO nanocomposite photoanode under sunlight irradiation.

the relative band positions of STO and ZFO, we used the Mott–Schottky relation:²⁶ $1/C^2 = (2/e\epsilon\epsilon_0N)[V_a - V_{fb} - kT/e]$, where C = space charge layers capacitance, e = electron charge, ϵ = dielectric constant, ϵ_0 = permittivity of vacuum, N = the charge carrier density, V_{ap} = applied potential, and V_{fb} = flat band potential. The signs of the slopes of the Mott–Schottky plots ($1/C^2$, as a function of V_{ap}) indicate that STO and ZFO are n-type (Figure 4c). V_{fb} values were determined by taking the x intercepts of linear fits to the Mott–Schottky plots. The V_{fb} of the ZFO film was 90 mV more negative than that of the STO film. The estimated energy band structures of the STO and ZFO (Figure 4e) were constructed on the basis of the Tauc plots and the Mott–Schottky plots and revealed a staggered energy band alignment.^{8,19,20} To understand the effect of the heterojunctions of STO:ZFO nanocomposites on the charge transfer in the PEC process, electrochemical impedance

spectroscopy (EIS) measurements were conducted under the same conditions where the photoanodes generated photocurrents. ZnFe_2O_4 is n-type, and the hole (minority carrier) diffusion length should be the photocurrent limiting process.²⁷ In other words, hole diffusion before carrier recombination plays an important role in the photoenergy conversion efficiency. Spatial separation of photogenerated carriers and extraction of the counter carriers (in this case, electrons) through the films by the nanoscale interdigitation of the materials is a strategy for increasing minority carrier lifetime. Figure 4d shows Nyquist plots obtained from potentiostatic EIS, where the x - and y -axes are the real part and the negative of the imaginary part of the impedance, respectively. To fit the measured EIS data, the Randles–Ershler model was adopted,²⁸ in which R_s is the electrolyte resistance, CPE is the capacitance phase element, and R_{ct} is the charge-transfer resistance of each photoelectrode. A smaller fitted value of R_{ct} and a larger fitted value of CPE represent improved charge transport characteristics.²⁹ The charge-transfer resistances R_{ct} in ZFO and STO:ZFO photoelectrodes were 8.03 and 1.92 k Ω , respectively, and their CPE values were 96.2 and 253.0 μF , respectively, which demonstrates the improved photogenerated charge carrier transfer in the STO:ZFO photoanodes (Figure 4e).

4. CONCLUSIONS

In summary, vertically aligned heteroepitaxial STO:ZFO nanocomposite films which form by spontaneous phase ordering yielded 7.9- and 2.6-fold higher PEC water oxidation efficiency under the solar simulator than the cases of individual STO and ZFO films, respectively. On the basis of the results from a series of measurements, the efficiency enhancement was shown to originate from improved photogenerated charge carrier transfer. Hence, this new kind of nanocomposite materials in the photocatalysis area gives very effective separation of photoexcited charge carriers as a result of (i) the vertical alignment of the phase-separated components, (ii) the single-crystalline nature of each phase, and (iii) the epitaxial heterojunctions. Here, only the compositions studied served as a first demonstration of the principle, but a large number of other material combinations in the nanocomposite, in the conducting layers, and in the underlying substrate are possible to achieve an even better solar energy conversion efficiency. Furthermore, self-assembled heteroepitaxial nanocomposites can also be prepared by solution-based methods beneficial to a large-scale synthesis.^{10,30,31} Therefore, this work represents a practical new approach to enhanced solar energy conversion as well as in other catalytic areas.

■ ASSOCIATED CONTENT

Supporting Information

The Supporting Information is available free of charge on the ACS Publications website at DOI: 10.1021/acs.chemmater.6b00122.

The ω - 2θ scan of a bare SrTiO_3 (STO) substrate and reciprocal space maps (RSMs) around the STO(002) and -(103) reflections of the STO substrate (Figure S1); ω - 2θ scan, reciprocal space map around the STO(103) reflections, and AFM image of STO: ZnFe_2O_4 (ZFO) nanocomposite film with ZFO overlayer on the SrRuO_3 (SRO)-buffered STO substrate (Figure S2); AFM image of ZFO film (Figure S3); relative absorbance spectra of

ZFO film and STO:ZFO nanocomposite film (Figure S4); and comparison of photocurrent densities with the corresponding integrated IPCE values (Table S1) (PDF)

AUTHOR INFORMATION

Corresponding Author

*E-mail: jld35@cam.ac.uk

Notes

The authors declare no competing financial interest.

ACKNOWLEDGMENTS

This work was supported by the European Research Council (ERC) (Advanced Investigator grant ERC-2009-AdG-247276-NOVOX).

REFERENCES

- (1) Walter, M. G.; Warren, E. L.; McKone, J. R.; Boettcher, S. W.; Mi, Q.; Santori, E. A.; Lewis, N. S. Solar Water Splitting Cells. *Chem. Rev.* **2010**, *110*, 6446–6473.
- (2) Hu, S.; Shaner, M. R.; Beardslee, J. A.; Lichtenman, M.; Brunschwig, B. S.; Lewis, N. S. Amorphous TiO₂ Coatings Stabilize Si, GaAs, and GaP Photoanodes for Efficient Water Oxidation. *Science* **2014**, *344*, 1005–1009.
- (3) Kronawitter, C. X.; Vayssieres, L.; Shen, S. H.; Guo, L. J.; Wheeler, D. A.; Zhang, J. Z.; Antoun, B. R.; Mao, S. S. A Perspective on Solar-Driven Water Splitting with All-Oxide Hetero-Nanostructures. *Energy Environ. Sci.* **2011**, *4*, 3889–3899.
- (4) Wang, Y.; Yu, T.; Chen, X. Y.; Zhang, H. T.; Ouyang, S. X.; Li, Z. S.; Ye, J. H.; Zou, Z. G. Enhancement of Photoelectric Conversion Properties of SrTiO₃/α-Fe₂O₃ Heterojunction Photoanode. *J. Phys. D: Appl. Phys.* **2007**, *40*, 3925–3930.
- (5) McDonald, K. J.; Choi, K. S. Synthesis and Photoelectrochemical Properties of Fe₂O₃/ZnFe₂O₄ Composite Photoanodes for Use in Solar Water Oxidation. *Chem. Mater.* **2011**, *23*, 4863–4869.
- (6) Hou, Y.; Li, X.-Y.; Zhao, Q.-D.; Quan, X.; Chen, G.-H. Electrochemical Method for Synthesis of a ZnFe₂O₄/TiO₂ Composite Nanotube Array Modified Electrode with Enhanced Photoelectrochemical Activity. *Adv. Funct. Mater.* **2010**, *20*, 2165–2174.
- (7) Park, J. H.; Park, O. O.; Kim, S. Photoelectrochemical Water Splitting at Titanium Dioxide Nanotubes Coated with Tungsten Trioxide. *Appl. Phys. Lett.* **2006**, *89*, 163106.
- (8) Boumazza, S.; Boudjemaa, A.; Bouguelia, A.; Bouarab, R.; Trari, M. Visible Light Induced Hydrogen Evolution on New Hetero-System ZnFe₂O₄/SrTiO₃. *Appl. Energy* **2010**, *87*, 2230–2236.
- (9) Qin, D.-D.; Tao, C.-L. A Nanostructured ZnO-ZnFe₂O₄ Heterojunction for the Visible Light Photoelectrochemical Oxidation of Water. *RSC Adv.* **2014**, *4*, 16968–16972.
- (10) Moshnyaga, V.; Damaschke, B.; Shapoval, O.; Belenchuk, A.; Faupel, J.; Lebedev, O. I.; Verbeeck, J.; van Tendeloo, G.; Mucksch, M.; Tsurkan, V.; Tidecks, R.; Samwer, K. Structural Phase Transition at the Percolation Threshold in Epitaxial (La_{0.7}Ca_{0.3}MnO₃)_{1-x}:(MgO)_x Nanocomposite Films. *Nat. Mater.* **2003**, *2*, 247–252.
- (11) Zheng, H.; Wang, J.; Lofland, S. E.; Ma, Z.; Mohaddes-Ardabili, L.; Zhao, T.; Salamanca-Riba, L.; Shinde, S. R.; Ogale, S. B.; Bai, F.; Viehland, D.; Jia, Y.; Schlom, D. G.; Wuttig, M.; Roytburd, A.; Ramesh, R. Multiferroic BaTiO₃-CoFe₂O₄ Nanostructures. *Science* **2004**, *303*, 661–663.
- (12) MacManus-Driscoll, J. L.; Foltyn, S. R.; Jia, Q. X.; Wang, H.; Serquis, A.; Civale, L.; Maiorov, B.; Hawley, M. E.; Maley, M. P.; Peterson, D. E. Strongly Enhanced Current Densities in Superconducting Coated Conductors of YBa₂Cu₃O_{7-x} + BaZrO₃. *Nat. Mater.* **2004**, *3*, 439–443.
- (13) MacManus-Driscoll, J. L.; Zerrer, P.; Wang, H.; Yang, H.; Yoon, J.; Fouchet, A.; Yu, R.; Blamire, M. G.; Jia, Q. Strain Control and Spontaneous Phase Ordering in Vertical Nanocomposite Heteroepitaxial Thin Films. *Nat. Mater.* **2008**, *7*, 314–320.
- (14) Harrington, S. A.; Zhai, J.; Denev, S.; Gopalan, V.; Wang, H.; Bi, Z.; Redfern, S. A. T.; Baek, S.-H.; Bark, C. W.; Eom, C.-B.; Jia, Q.; Vickers, M. E.; MacManus-Driscoll, J. L. Thick Lead-Free Ferroelectric Films with High Curie Temperatures through Nanocomposite-Induced Strain. *Nat. Nanotechnol.* **2011**, *6*, 491–495.
- (15) Fix, T.; Choi, E.-M.; Robinson, J. W. A.; Lee, S. B.; Chen, A.; Prasad, B.; Wang, H.; Blamire, M. G.; MacManus-Driscoll, J. L. Electric-Field Control of Ferromagnetism in a Nanocomposite via a ZnO Phase. *Nano Lett.* **2013**, *13*, 5886–5890.
- (16) Kursumovic, A.; Defay, E.; Lee, O. J.; Tsai, C.-F.; Bi, Z.; Wang, H.; MacManus-Driscoll, J. L. A New Material for High-Temperature Lead-Free Actuators. *Adv. Funct. Mater.* **2013**, *23*, 5881–5886.
- (17) Su, Q.; Yoon, D.; Chen, A.; Khatkhatay, F.; Manthiram, A.; Wang, H. Vertically Aligned Nanocomposite Electrolytes with Superior Out-of-Plane Ionic Conductivity for Solid Oxide Fuel Cells. *J. Power Sources* **2013**, *242*, 455–463.
- (18) MacManus-Driscoll, J. L. Self-Assembled Heteroepitaxial Oxide Nanocomposite Thin Film Structures: Designing Interface-Induced Functionality in Electronic Materials. *Adv. Funct. Mater.* **2010**, *20*, 2035–2045.
- (19) Dom, R.; Subasri, R.; Hebalkar, N. Y.; Chary, A. S.; Borse, P. H. Synthesis of a Hydrogen Producing Nanocrystalline ZnFe₂O₄ Visible Light Photocatalyst Using a Rapid Microwave Irradiation Method. *RSC Adv.* **2012**, *2*, 12782–12791.
- (20) Li, J.; Wu, N. Semiconductor-Based Photocatalysts and Photoelectrochemical Cells for Solar Fuel Generation: A Review. *Catal. Sci. Technol.* **2015**, *5*, 1360–1384.
- (21) Cho, S.; Jang, J.-W.; Zhang, W.; Suwardi, A.; Wang, H.; Wang, D.; MacManus-Driscoll, J. L. Single-Crystalline Thin Films for Studying Intrinsic Properties of BiFeO₃-SrTiO₃ Solid Solution Photoelectrodes in Solar Energy Conversion. *Chem. Mater.* **2015**, *27*, 6635–6641.
- (22) Kim, J. H.; Kim, J. H.; Jang, J.-W.; Kim, J. Y.; Choi, S. H.; Magesh, G.; Lee, J.; Lee, J. S. Awakening Solar Water-Splitting Activity of ZnFe₂O₄ Nanorods by Hybrid Microwave Annealing. *Adv. Energy Mater.* **2015**, *5*, DOI: 10.1002/aenm.201401933.
- (23) Dom, R.; Kumar, G. S.; Hebalkar, N. Y.; Joshi, S. V.; Borse, P. H. Eco-Friendly Ferrite Nanocomposite Photoelectrode for Improved Solar Hydrogen Generation. *RSC Adv.* **2013**, *3*, 15217–15224.
- (24) Joshi, U. A.; Jang, J. S.; Borse, P. H.; Lee, J. S. Microwave Synthesis of Single-Crystalline Perovskite BiFeO₃ Nanocubes for Photoelectrode and Photocatalytic Applications. *Appl. Phys. Lett.* **2008**, *92*, 242106.
- (25) Ji, W.; Yao, K.; Lim, Y.-F.; Liang, Y. C.; Suwardi, A. Epitaxial Ferroelectric BiFeO₃ Thin Films for Unassisted Photocatalytic Water Splitting. *Appl. Phys. Lett.* **2013**, *103*, 062901.
- (26) Cardon, F.; Gomes, W. P. On the Determination of the Flat-Band Potential of a Semiconductor in Contact with a Metal or an Electrolyte from the Mott-Schottky Plot. *J. Phys. D: Appl. Phys.* **1978**, *11*, L63–L67.
- (27) Sheikh, A.; Yengantiwar, A.; Deo, M.; Kelkar, S.; Ogale, S. Near-Field Plasmonic Functionalization of Light Harvesting Oxide–Oxide Heterojunctions for Efficient Solar Photoelectrochemical Water Splitting: The AuNP/ZnFe₂O₄/ZnO System. *Small* **2013**, *9*, 2091–2096.
- (28) Yuan, X.; Song, C.; Wang, H.; Zhang, J. *Electrochemical Impedance Spectroscopy in PEM Fuel Cells: Fundamentals and Applications*; Springer: London, U.K., 2010.
- (29) Jo, W. J.; Jang, J.-W.; Kong, K.-j.; Kang, H. J.; Kim, J. Y.; Jun, H.; Parmar, K. P. S.; Lee, J. S. Phosphate Doping into Monoclinic BiVO₄ for Enhanced Photoelectrochemical Water Oxidation Activity. *Angew. Chem., Int. Ed.* **2012**, *51*, 3147–3151.
- (30) Lebedev, O. I.; Verbeeck, J.; van Tendeloo, G.; Shapoval, O.; Belenchuk, A.; Moshnyaga, V.; Damaschke, B.; Samwer, K. Structural Phase Transitions and Stress Accommodation in (La_{0.67}Ca_{0.33}MnO₃)_{1-x}:(MgO)_x composite films. *Phys. Rev. B: Condens. Matter Mater. Phys.* **2002**, *66*, 104421.

(31) Liu, B.; Sun, T.; He, J.; Dravid, V. P. Sol-Gel-Derived Epitaxial Nanocomposite Thin Films with Large Sharp Magnetoelectric Effect. *ACS Nano* **2010**, *4*, 6836–6842.